Investigations on thermo-mechanical modeling of abradable coating in the context of rotor/stator interactions

Florence Nyssen, Alain Batailly

Investigations on thermo-mechanical modeling of abradable coating in the context of rotor/stator interactions

Nyssen F.[1], Batailly A.[1]

Abstract
In modern turbomachine designs, the nominal clearances between rotating bladed-disks and the surrounding casings are reduced to improve aerodynamical performances. But the reduction of nominal clearances significantly increases the risk of occurrence of contacts between static and rotating components and may lead to hazardous interaction phenomena. A common technical solution to mitigate this issue consists in the addition of an abradable coating on the casing inner surface. Even so, contact interactions between the blade tips and this abradable coating may yield unexpected abradable wear removal phenomena. For that reason, recent researches have focused on the numerical simulation of rotor/stator interactions with wear removal mechanism of operating clearances while neglecting thermal effects. However, high temperature areas due to contact occurrence have been observed experimentally. These high temperatures are suspected to generate a self-excitation of the system due the abradable dilatation. Accordingly, the aim of this work is to investigate the numerical modeling of thermal effects in the abradable coating due to contact interactions.

Keywords
thermal effects; abradable coating; rotor/stator interaction

1 - Department of Mechanical Engineering, École Polytechnique de Montréal, P.O. Box 6079, Succ. Centre-Ville, Montréal, Québec, Canada H3C 3A7

Investigations sur la modélisation thermo-mécanique du revêtement abradable dans le contexte d'interactions rotor/stator

Nyssen F.[1], Batailly A.[1]

Résumé
Dans les conceptions modernes de turbomachines, les jeux nominaux entre les disques aubagés tournants et le carter environnant sont réduits pour améliorer les performances aérodynamiques. Mais la réduction des jeux nominaux augmente significativement le risque de contacts entre les composants statiques et rotatifs, et peut mener à des phénomènes dangereux d'interactions. Une solution technique usuelle pour réduire ce problème consiste dans l'ajout d'une couche abradable sur la surface intérieure du carter. Des interactions de contact entre le bout des aubes et cette couche abradable peuvent mener à un phénomène d'usure imprévu. Pour cette raison, des recherches récentes se sont focalisées sur la simulation numérique des interactions rotor/stator avec des mécanismes d'usure des jeux en fonctionnement, en négligeant les effets thermiques. Cependant, des zones de hautes températures dues à des contacts ont été observées expérimentalement. Ces hautes températures sont suspectées de générer une auto-excitation du système due à la dilatation de l'abradable. Par conséquent, le but de ce travail est d'investiguer la modélisation numérique des effets thermiques dans la couche abradable suite à des interactions de contact.

Mots-clés
effets thermiques; revêtement abradable; interactions rotor/stator

1 - Département de génie mécanique, École Polytechnique de Montréal, P.O. Box 6079, Succ. Centre-Ville, Montréal, Québec, Canada H3C 3A7

Introduction

Improving engine performances while lowering operating costs is a major issue for turbomachine manufacturers [1]. Also, environmental constraints are playing a prevailing role in modern engine designs, leading to an emphasis on reducing fuel consumptions. Modern technologies have been developed, allowing for: (1) the increase of operating temperatures, (2) the increase of casing conicity which enhances compression rates, (3) the use of lighter materials, as well as (4) more aerodynamically efficient designs. A solution to improve the aerodynamical performances of the engine consists in the reduction of the nominal clearances between the rotating bladed components (rotor) and the surrounding casing (stator). However, the reduction of the clearance between the tip of the blades and the stator increases the risk of occurrence of unilateral contacts between static and rotating components that may lead to hazardous interaction phenomena. Depositing a sacrificial abradable coating along the casing contact surface is a common technical solution to avoid these interactions [2, 3, 4]. But contact interactions between the blade-tips and the abradable coating may lead to unexpected abradable wear removal phenomena through various mechanisms, such as thermal gradient in the casing, coincidence of vibration modes, rotor imbalance resulting from design uncertainties, or whirl motions following maneuver loads [5]. For that reason, different researches have been carried on the blade dynamics in the context of unilateral and frictional contacts [6, 7, 8]. In particular, recent works have focused on the numerical simulation of rotor/stator interactions with wear removal mechanism [3, 9, 10, 5], neglecting thermal effects. But high temperature areas due to contact occurrences have been observed experimentally [11]. It is assumed that these high temperatures could generate a self-excitation of the system due to the abradable dilatation.

The aim of the proposed work is to investigate the numerical modeling of thermal effects in the abradable coating due to contact interactions. The first section of the article focuses on the theoretical description of the numerical models of the different system components (the blade, the abradable layer with wear and thermal modeling, and the casing), the contact model and the time integration algorithm. Space and time discretizations for the resolution of the thermal problem are also detailed, with emphasis on the reduction of computation times. In the second section, the proposed approach is applied on an industrial finite element model of a low-pressure compressor blade, and convergence analyses are carried out. More particularly, the effects of the spatial discretization and time step are studied for the thermal model. In the last section of the article, the obtained results are analyzed.

1 MODELING

The proposed work deals with a single rotating blade and the casing on which an abradable layer is deposited to accept physical contact events. Figure 1 summarizes the different components involved in the modeling. Because of the possibly large size of the finite element model of the bladed structure, a reduced order model (ROM) of the blade is used here, embedding centrifugal effects. Only a reduced number of boundary nodes are kept in the ROM at the contact interface along the blade tip. The abradable layer is modeled using one-dimensional two-node rod elements, which are mechanically independent of their adjacent neighbors. The model of the material removing for the abradable layer consist in a piecewise linear plastic constitutive law [5]. In addition to the mechanical mesh used to determine wear evolution, a thermal finite element mesh is added here to compute the temperature evolution in the abradable. When contact interactions occur, a heat flux is transmitted from the blade to the abradable, increasing the temperature of the impacted abradable elements. Then, the heat is conducted inside the abradable layer. The temperature variations induce dilatation of the abradable elements. Finally, the surrounding casing is modeled as a rigid component that remains insensitive to the contact interaction with the blades. A detailed description of each numerical model is given in this section.

1.1 Blade modeling

The governing equation of motion is given by:

$$\mathbf{M}\ddot{\mathbf{q}} + \mathbf{D}\dot{\mathbf{q}} + \mathbf{K}(\Omega)\,\mathbf{q} + \mathbf{F}^c(\mathbf{q}) = \mathbf{F}^e \tag{1}$$

where Ω is the angular speed, $\mathbf{q}$ stores the displacement of blade degrees of freedom, $\mathbf{M}$, $\mathbf{D}$ and $\mathbf{K}$ denote respectively the mass, damping and stiffness matrices, $\mathbf{F}^c$ contains the contact forces and $\mathbf{F}^e$ the external forces.

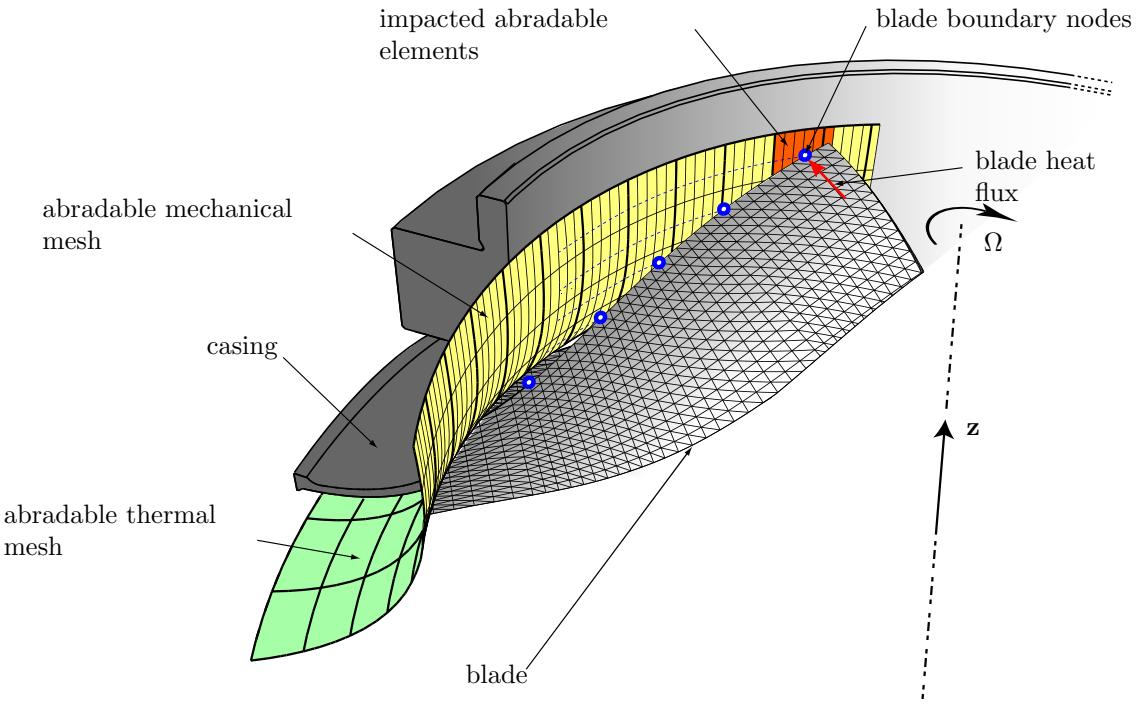

Figure 1. Representation of the thermal mesh and blade heat flux

In operating conditions, the blade tip will move due to centrifugal loadings. These centrifugal effects affect the computation of the stiffness matrix. As a first approximation, since the angular speed Ω is constant, the stiffness matrix can be written as a polynomial expansion over the rotational speed such as [12]:

$$\mathbf{K}(\Omega) = \mathbf{K}_0 + \Omega^2 \mathbf{K}_1 + \Omega^4 \mathbf{K}_2 \tag{2}$$

where the matrices $\mathbf{K}_0$, $\mathbf{K}_1$ and $\mathbf{K}_2$ are obtained by computing Eq. (2) for three values of the angular speed Ω, for instance, with $\Omega = 0, \Omega_{\max}/2$ and $\Omega_{\max}$. In this case, the three matrices can be expressed as [12, 13]:

$$\mathbf{K}_0 = \mathbf{K}(0) \tag{3}$$

$$\mathbf{K}_1 = \frac{1}{3\Omega_{\max}^2}\left(16\mathbf{K}\left(\frac{\Omega_{\max}}{2}\right) - \mathbf{K}(\Omega_{\max}) - 15\mathbf{K}(0)\right) \tag{4}$$

$$\mathbf{K}_2 = \frac{4}{3\Omega_{\max}^4}\left(\mathbf{K}\left(\frac{\Omega_{\max}}{2}\right) - 4\mathbf{K}(\Omega_{\max}) + 3\mathbf{K}(0)\right) \tag{5}$$

Because of the large size of the finite element model of the bladed structure, ROMs are used for explicit time integration simulations. The transformation matrix $\mathbf{\Phi}$ enables to reduce the size of the model:

$$\mathbf{\Phi} = \begin{bmatrix} \mathbf{I} & \mathbf{0} \\ \mathbf{\Phi}_R(0) & \mathbf{\Psi} \end{bmatrix} \tag{6}$$

with:

$$\mathbf{\Psi} = \begin{bmatrix} \mathbf{\Phi}_R\left(\frac{\Omega_m}{2}\right)^\star \\ \mathbf{\Phi}_R\left(\Omega_m\right)^\star \\ \mathbf{\Phi}_L\left(0\right) \\ \mathbf{\Phi}_L\left(\frac{\Omega_m}{2}\right) \\ \mathbf{\Phi}_L\left(\Omega_m\right) \end{bmatrix}^\mathsf{T} \tag{7}$$

in which $\mathbf{\Phi}_R\left(\Omega\right)$ and $\mathbf{\Phi}_L\left(\Omega\right)$ stand respectively for n_c constraint modes and η fixed interface modes computed for a rotation speed Ω. The superscript $\star$ indicates that matrix $\mathbf{\Phi}_R\left(0\right)$ is substracted. An orthonormalization of the matrix $\mathbf{\Psi}$ is performed to avoid potential rank-deficiency due to similarities between the constraint modes. The maximum size of the reduced-order model is therefore equal to $3n_c + 3\eta$.

1.2 Contact interactions

The contact force vector $\mathbf{F}^c\left(\mathbf{q}\right)$ is computed using Lagrange multipliers [14, 15]. The blade is considered as the master surface Γ_c^m, and the abradable layer the slave surface Γ_c^s. For any material point of the blade $\mathbf{x} \in \Gamma_c^m$ (restricted here to the interface nodes at the blade tip), it is possible to find the closest counterpart $\bar{\mathbf{y}}$ on the the abradable slave surface:

$$\bar{\mathbf{y}} = \arg\min_{y \in \Gamma_e^s} \|\mathbf{x} - \mathbf{y}\| \tag{8}$$

Using these notations, the discretized clearance between the blade and the abradable can be written as:

$$\mathbf{g}\left(\mathbf{x}\right) = \mathbf{g}_0\left(\mathbf{x}\right) + \left(\mathbf{u}^m\left(\mathbf{x}\right) - \mathbf{u}\left(\bar{\mathbf{y}}(\mathbf{x})\right)\right) \cdot \mathbf{n} \tag{9}$$

in which $\mathbf{g}_0\left(\mathbf{x}\right)$ is the initial positive gap, $\mathbf{n}$ is the outward normal to the slave surface Γ_c^s. Regarding to the Kuhn-Tucker optimality conditions, the contact conditions are:

$$\forall \mathbf{x} \in \Gamma_c^s, \mathbf{t}_N \geq 0, \mathbf{g}(\mathbf{x}) \geq 0, \mathbf{t}_N \mathbf{g}(\mathbf{x}) = 0 \tag{10}$$

in which $\mathbf{t}_N$ denotes the discretized contact pressure which is positive when acting on the contact interface.

1.3 Abradable coating modeling

A weak thermo-mechanical coupling is assumed for the abradable coating modeling, meaning that thermal effects affect the system mechanics, but the mechanical deformation of the element has no effect on temperatures. Since mechanics has no effect on thermics, the conduction problem can be first solved separately. Weak coupling is well appropriated in the case of rapid dynamics using small time steps and explicit resolution schemes [16]. Moreover, only heat transfer by conduction is considered in this work, convection and radiation effects can be neglected because of their lower contribution to heat transfer in the studied case. The detailed description of the mechanical and thermal model is given in this section.

1.3.1 Mechanical modeling

The abradable coating is modeled using one-dimentional two-node rod elements as illustrated in Figure 2. Each element is mechanically independent of its adjacent neighbors. Over the thickness of the abradable layer, a single element is used since calculations are performed in a quasi-static framework. It is assumed that the abradable elements undergo both elastic ε_e and plastic deformations ε_p following the contact with the blade such as $\varepsilon = \varepsilon_e + \varepsilon_p$. The plastic constitutive law, illustrated in Figure 3, enables to compute the normal forces exerted by the blade onto the abradable coating elements and the evolution of the abradable coating profile through permanent plastic deformation. The set of admissible stresses $\mathbb{E}_\sigma$ is given by:

$$\mathbb{E}_\sigma = \{(\sigma, \alpha) \in (\mathbb{R}, \mathbb{R}) \,|\, f\left(\sigma, \alpha\right) \leq 0\} \tag{11}$$

with α the internal hardening variable and f the yield function. The relation between elastic strains ε_e and stresses σ is assumed linear, such as $\sigma = E\varepsilon_e$ with E the abradable Young's modulus. The hardening is assumed isotropic, which corresponds to a uniform expansion of the initial yield surface without translation. The center of the yield surface does not move. The yield function is defined as:

$$f(\sigma, \alpha) = \sigma - (\sigma_Y + K\alpha) \tag{12}$$

in which σ_Y is the elastic limit and K is the plastic modulus.

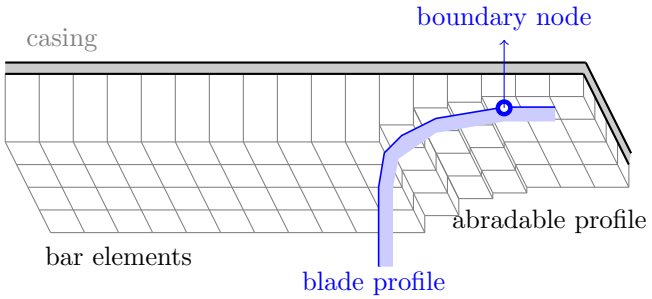

Figure 2. Abradable coating modeling

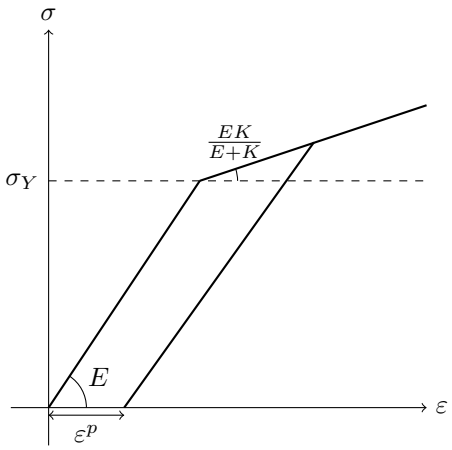

Figure 3. Plasticity constitutive law of the abradable mechanical elements

1.3.2 Thermal modeling

In addition to the mechanical mesh used to determine the time evolution of the displacement field, a thermal finite element mesh is associated in this work to the abradable coating. Each node of the thermal mesh has one degree of freedom, the temperature of the element. The temperature field in the abradable coating $\mathbf{T}(x, y, z, t)$ reads:

$$\mathbf{T}(x, y, z, t) = \mathbf{N}(x, y, z)\ \mathbf{T}(t) \tag{13}$$

where $\mathbf{N}(x, y, z)$ is the interpolation function matrix and $\mathbf{T}(t)$ contains the nodal temperatures. The heat equation is given by:

$$\mathbf{C}_T\dot{\mathbf{T}} + \mathbf{K}_T\mathbf{T} = \mathbf{F}_T \tag{14}$$

in which:

- the thermal capacity matrix $\mathbf{C}_T$ (in $\mathrm{J{\cdot}K^{-1}}$) reads:

$$\mathbf{C}_T = \int_V \rho c_P \mathbf{N}^T \mathbf{N} dV \tag{15}$$

with ρ the abradable density (in $\mathrm{kg{\cdot}m^{-3}}$) and c_P the thermal capacity (in $\mathrm{J{\cdot}kg^{-1}{\cdot}K^{-1}}$);

- the thermal conductibility matrix $\mathbf{K}_T$ (in $\mathrm{W{\cdot}K^{-1}}$) is given by:

$$\mathbf{K}_T = \int_V \mathbf{B}^T \lambda \mathbf{B} dV \tag{16}$$

with

$$\mathbf{B} = \begin{bmatrix} \frac{\partial N_1}{\partial x} & \dots & \frac{\partial N_n}{\partial x} \\ \frac{\partial N_1}{\partial y} & \dots & \frac{\partial N_n}{\partial y} \\ \frac{\partial N_1}{\partial z} & \dots & \frac{\partial N_n}{\partial z} \end{bmatrix} \tag{17}$$

and $\boldsymbol{\lambda}$ the conductivity matrix, which reads, for an isotropic material (λ is the thermal conductivity coefficient of the abradable coating, in $\mathrm{W{\cdot}m^{-1}{\cdot}K^{-1}}$):

$$\boldsymbol{\lambda} = \lambda \begin{bmatrix} 1 & 0 & 0 \\ 0 & 1 & 0 \\ 0 & 0 & 1 \end{bmatrix} \tag{18}$$

- the nodal heat flux vector $\mathbf{F}_T$ (in W) is given by:

$$\mathbf{F}_T = \mathbf{Q} + \int_V \mathbf{N}^T \mathbf{q} dV \tag{19}$$

with $\mathbf{Q}$ the punctual nodal heat flux (in W) and $\mathbf{q}$ the volumetric heat flux (in $\mathrm{W{\cdot}m^{-3}}$). By convention, the heat flux received by the solid is counted as positive. Only punctual nodal forces are considered in the following.

To reduce computation times, a coarser spatial discretization is used for the thermal mesh comparing to the mechanical one. As illustrated in Figure 4, there is one thermal element for R_s mechanical elements. Therefore, an impact on the R_s mechanical elements will provide a heat flux for the considered thermal element.

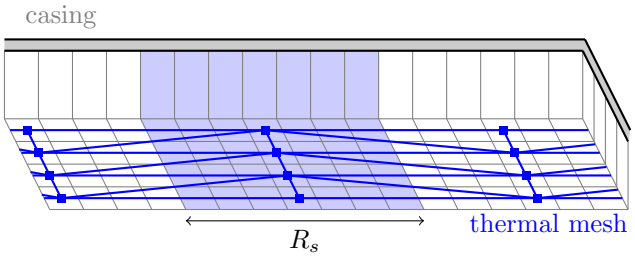

Figure 4. Space discretization of the thermal abradable mesh comparing to the mechanical one

Triangular elements are considered for convenience to build the thermal mesh. Considering an element with three nodes of coordinates (x_1, y_1), (x_2, y_2) et (x_3, y_3) respectively, the temperature field in the element reads:

$$\begin{aligned} T(x) &= N_1(x,y)T_1 + N_2(x,y)T_2 + N_3(x,y)T_3 \\ &= [N_1(x,y)\ N_2(x,y)\ N_3(x,y)] \begin{bmatrix} T_1 \\ T_2 \\ T_3 \end{bmatrix} \end{aligned} \tag{20}$$

in which (noting $y_{ab} = (y_a - y_b)$, $x_{ab} = (x_a - x_b)$ with $a, b = 1, 2, 3$):

$$\begin{aligned} N_1(x,y) &= \frac{1}{2A^e}\left(y_{32}\left(x_2 - x\right) - x_{32}\left(y_2 - y\right)\right) \\ N_2(x,y) &= \frac{1}{2A^e}\left(y_{13}\left(x_3 - x\right) - x_{13}\left(y_3 - y\right)\right) \\ N_3(x,y) &= \frac{1}{2A^e}\left(y_{21}\left(x_1 - x\right) - x_{21}\left(y_1 - y\right)\right) \end{aligned} \tag{21}$$

with A^e the surface of the element, given by:

$$A^e = \frac{x_{21}y_{31} - x_{31}y_{21}}{2} \tag{22}$$

Using these interpolation functions leads to:

$$\mathbf{B} = \frac{1}{2A^e}\begin{bmatrix} y_{23} & y_{31} & y_{12} \\ x_{32} & x_{13} & x_{21} \end{bmatrix} \tag{23}$$

and:

- the elementary thermal conductibility matrix $\mathbf{K}_T^e$ reads:

$$\mathbf{K}_T^e = \frac{\lambda}{4A^e} \begin{bmatrix} y_{23}^2 + x_{32}^2 & y_{23}y_{31} + x_{32}x_{13} & y_{23}y_{12} + x_{32}x_{21} \\ y_{31}y_{23} + x_{13}x_{32} & y_{31}^2 + x_{13}^2 & y_{31}y_{12} + x_{13}x_{21} \\ y_{12}y_{23} + x_{21}x_{32} & y_{12}y_{31} + x_{21}x_{13} & y_{12}^2 + x_{21}^2 \end{bmatrix} \tag{24}$$

- the elementary thermal capacity matrix $\mathbf{C}_T^e$ is given by:

$$\mathbf{C}_T^e = \frac{\rho c_P A_e}{12}\begin{bmatrix} 2 & 1 & 1 \\ 1 & 2 & 1 \\ 1 & 1 & 2 \end{bmatrix} \tag{25}$$

- the elementary heat vector $\mathbf{F}_T^e$ due to a volumic source of intensity q reads:

$$\mathbf{F}_T^e = \frac{qA^e}{4}\begin{bmatrix} 1 \\ 1 \\ 1 \end{bmatrix} \tag{26}$$

Matrices $\mathbf{C}_T$, $\mathbf{K}_T$ and $\mathbf{F}_T$ are then constructed by assembling the elementary matrices.

Denoting by subscript L the degrees of freedom of unknown temperature and by subscript P the nodes where the temperature is known, the thermal conductivity matrix, capacity matrix and heat vector can be partitioned, such as:

$$\mathbf{C}_T = \begin{bmatrix} \mathbf{C}_{LL} & \mathbf{C}_{LP} \\ \mathbf{C}_{PL} & \mathbf{C}_{PP} \end{bmatrix}, \mathbf{K}_T = \begin{bmatrix} \mathbf{K}_{LL} & \mathbf{K}_{LP} \\ \mathbf{K}_{PL} & \mathbf{K}_{PP} \end{bmatrix}, \mathbf{F}_T = \begin{bmatrix} \mathbf{F}_L \\ \mathbf{F}_P \end{bmatrix} \tag{27}$$

The temperature at a given time $t + 1$ can be determined using the following equation system [17]:

$$\begin{aligned} &\bar{\mathbf{K}}_{LL}\Delta\mathbf{T}_L = \bar{\mathbf{F}}_L(t) \\ &\mathbf{T}_L(s+1) = \mathbf{T}_L(s) + \Delta\mathbf{T}_L \end{aligned} \tag{28}$$

with:

$$\begin{aligned}\bar{\mathbf{K}}_{LL} &= \mathbf{C}_{LL} + \beta\ \Delta t\ \mathbf{K}_{LL} \\ \bar{\mathbf{F}}_L(t) &= \Delta t \left(\mathbf{F}_L(t) - \mathbf{C}_{LP}\dot{\mathbf{T}}_P(t) - \mathbf{K}_{LP}\mathbf{T}_P(t) - \mathbf{K}_{LL}\mathbf{T}_L(s)\right)\end{aligned} \tag{29}$$

and the initial conditions $\mathbf{T}\,(t=0) = \mathbf{T}_0$. β denotes the parameter of the integration scheme and Δt is the time step. $\mathbf{F}$ contains the heat sources, in this case the heat transmitted by the blade to the abradable coating during contact phase, as illustrated in Figure 1. In this preliminary study, the heat flux is assumed proportional to the amount of removed abradable. The temperature is assumed to be unknown in all abradable elements, except at the initial time. Therefore, the set P of degrees of freedom of known temperature is empty in this particular case.

Denoting ω_{max} the largest eigenfrequency of $\mathbf{C}^{-1}\mathbf{K}$, one can demonstrates [17] that the integration scheme is stable for $\Delta t < \frac{2}{(1-2\beta)\omega_{max}}$, unconditionally stable for $\beta \geq \frac{1}{2}$, and stable without oscillation for $\Delta t < \frac{2}{(1-\beta)\omega_{max}}$.

Knowing the temperature evolution in the abradable coating, the displacement field can be updated by computing the element dilatation. Assuming a linear thermo-elastic constitutive law leads to:

$$\varepsilon_T = \alpha_T \Delta T \tag{30}$$

in which ε_T is the thermal deformation, α_T is the thermal expansion coefficient and ΔT is the temperature variation.

1.4 Time integration

To compute the displacement of the blade and the abradable wear, an explicit time integration procedure is used in the paper, based on the central finite-differences method. At each iteration n, displacements $\mathbf{x}_{n+1}$ are linearly predicted using the following scheme:

$$\mathbf{x}^p_{n+1} = \mathbf{A}\mathbf{x}_n + \mathbf{B}\mathbf{x}_{n-1} \tag{31}$$

with

$$\mathbf{A} = \left[\frac{\mathbf{M}}{h^2} + \frac{\mathbf{D}}{2h}\right]^{-1}\left[\frac{2\mathbf{M}}{h^2} - \mathbf{K}\right] \tag{32}$$

$$\mathbf{B} = \left[\frac{\mathbf{M}}{h^2} + \frac{\mathbf{D}}{2h}\right]^{-1}\left[\frac{\mathbf{D}}{2h} - \frac{\mathbf{M}}{h^2}\right] \tag{33}$$

If a contact interaction is detected at the time step n, predicted displacements are corrected such as:

$$\mathbf{x}_{n+1} = \mathbf{x}^p_{n+1} + \mathbf{C}\boldsymbol{\lambda} \tag{34}$$

where $\boldsymbol{\lambda}$ denotes the contact forces and $\mathbf{C} = \left[\frac{\mathbf{M}}{h^2} + \frac{\mathbf{D}+\mathbf{G}}{2h}\right]^{-1}$.

Since the time constant of thermal effect is larger than the one of contact interactions, a different time discretization is used to compute the evolution of abradable temperature. Instead of computing the temperature evolution at each time step, the thermal equation is solved every R_t mechanical time steps. The heat flux applied at each thermal time step is equal to the sum of the flux applied on the considered element along the R_t last mechanical time steps (as illustrated schematically in Figure 5). This enables to significantly reduce computation times. The dilatation of

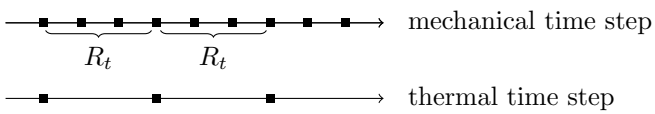

Figure 5. Time discretization of the thermal equations comparing to the mechanical ones

the abradable mechanical elements due to the increase of temperature computed every R_t time step is applied every thermal time step since the increase of temperature are small. The different steps of the time integration algorithm is summarized in Figure 6.

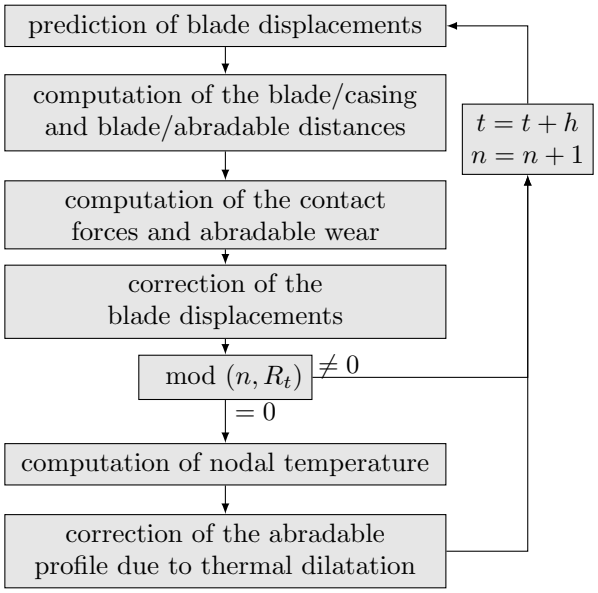

Figure 6. Time integration algorithm

2 VALIDATION ON AN INDUSTRIAL MODEL

Numerical simulations are performed on a low pressure compressor blade, shown in Figure 7. Eight nodes along the blade tip are considered at the contact interface in the reduced order model (red dots in Figure 7). Ten modes are retained in the ROM. The rotational speed of the blade is assumed constant and equal to 450 rad·s^{-1}. The number of mechanical abradable element is fixed to 5000. The thermal dilatation coefficient is equal to $5 \cdot 10^{-6}$ K^{-1}, the thermal capacity to 1 J·kg^{-1}·K^{-1} and the thermal conductivity to 1 W·K^{-1}. $\beta = 0.5$ for the thermal iteration scheme.

The contact between the blade and the surrounding casing is initiated by applying quasi-statically a two-lobe deformation of the casing in order to absorb the initial clearances. The different simulations are conducted on 10 rounds of the blades.

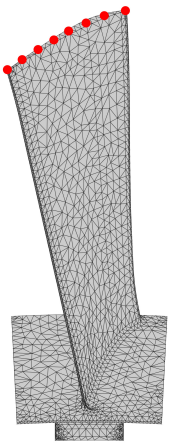

Figure 7. Studied structure with the nodes retained in the reduced order model in red

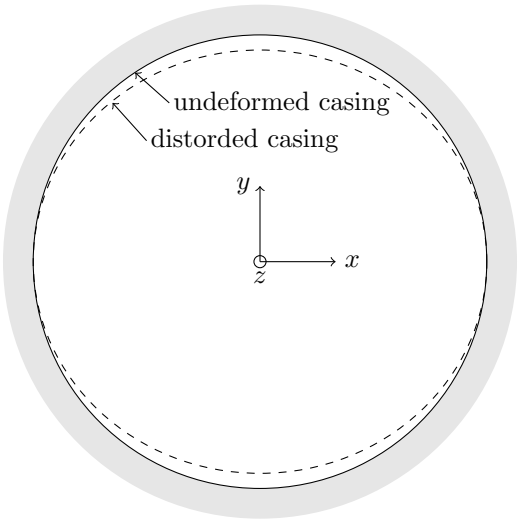

Figure 8. Two-lobe deformation of the casing

2.1 Spatial convergence

Figures 9a and 9b show the spatial convergence of the temperature profile in the abradable coating after 10 rotations of the blade for the leading edge and the trailing edge respectively. 1000, 100 and 50 elements are considered along the circumference of the abradable layer (this corresponds to $R_s = 5$, 50 and 100 respectively). The number of mechanical abradable elements is kept equal to 5000. A good convergence of the temperature profile is observed and 50 thermal elements along the circumference can be kept. The reduction of the number of thermal elements enables to decrease the size of the thermal problem (Equation (28)) and efficiently reduce computation times.

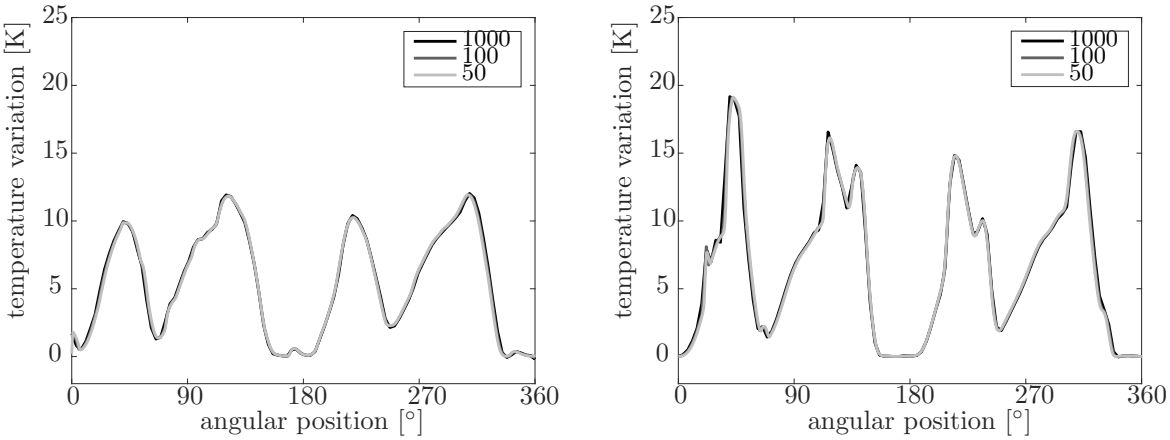

(a) Leading edge

(b) Trailing edge

Figure 9. Convergence of the temperature profile along the abradable circumference for different numbers of thermal abradable elements

2.2 Time convergence

Figures 10a and 10b show the time convergence of the temperature profile in the abradable coating after 10 rotations of the blade for the leading edge and the trailing edge respectively. It is observed that when R_t increases, *i.e.* the time discretization increases, the temperature increases at the leading edge and the temperature decreases at the

trailing edge. This can be explained by the delay of the conduction inside of the abradable coating. A schematic illustration explaining this effect is given in Figure 11. It is considered here that the blade enters in contact with the abradable at the mechanical time step 1 at the leading edge. If the thermal time step is equal to the mechanical time step, the temperature of the abradable increases at the mechanical time step 1 at the leading edge. Then, the temperature progressively decreases at the leading edge at the next time steps and the temperature slightly increase at the trailing edge by conduction. However, if the thermal time step is equal to two times the mechanical time step, the heat flux generated by the blade at the mechanical time step 1 will be applied at time step 2, and the temperature of the abradable increases at the mechanical time step 2 at the leading edge. Then, the temperature progressively decreases at the leading edge at the next time steps and the temperature slightly increases at the trailing edge by conduction. Therefore, when the thermal time step increases comparing the mechanical time step, the temperature will be slightly higher at the leading edge and slightly lower at the trailing edge due to conduction time.

The obtained temperature profile in the abradable is therefore more sensitive to the time discretization than to the space discretization. In the following, the time discretization parameter R_t is fixed to 50.

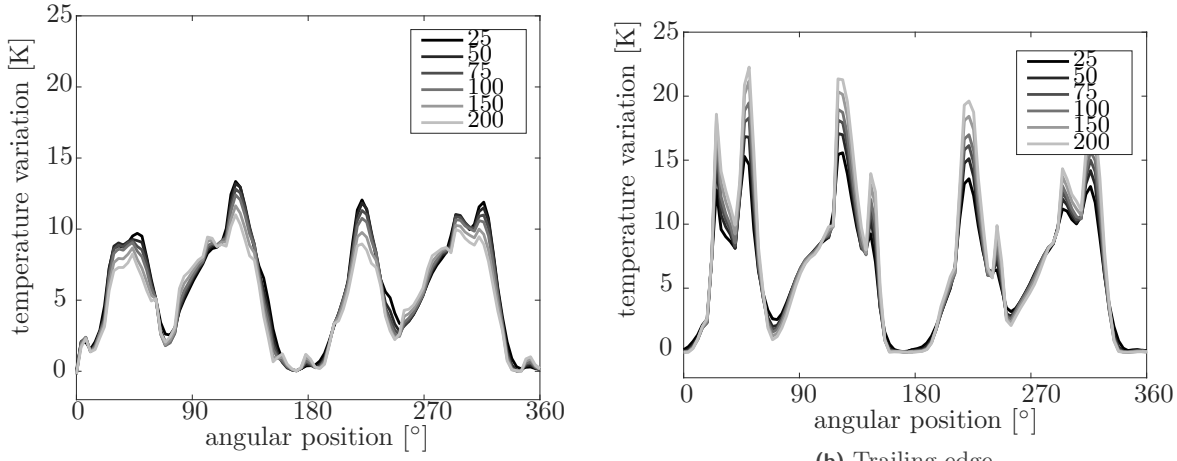

(a) Leading edge **(b)** Trailing edge

Figure 10. Time convergence of the temperature profile along the abradable circumference for different values of R_t

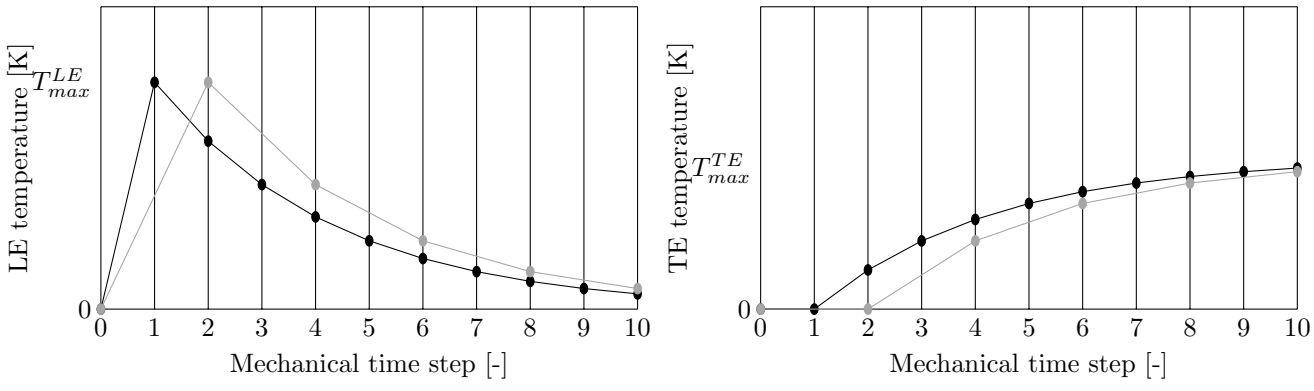

(a) Leading edge **(b)** Trailing edge

Figure 11. Schematic explanation of the time convergence at the leading edge (LE) and trailing edge (TE). Black curve: $R_t = 1$, gray curve: $R_t = 2$.

2.3 Results

Figures 12 and 13 show respectively the time evolution of wear and temperature over the circumference of the abradable at the leading and trailing edges. In the first graph, a planar representation is given. The horizontal axis corresponds to the mechanical time step, the vertical axis corresponds to the angular position of the abradable element. The color scale gives the normalized wear amplitude (Figure 12) and temperature (Figure 13). The second graph gives the normalized wear profile in polar coordinates for different time steps. Lighter lines correspond to first time steps and darker curves to last mechanical time steps.

At the leading edge, two contact areas are observed, leading to two wear lobes. For the last time steps, a small contribution of four wear lobes is observed. At the trailing edge, four contact lobes are obtained. These contact areas bring heat from the blades to the abradable layer. Two temperature peaks areas are observed at the leading edge, while four temperature peaks areas can be seen at the trailing edge. The heat is then transmitted in the abradable layer by conduction. Along time, a uniform temperature distribution is observed at both leading and trailing edges, and four higher temperature areas are observed on both edges.

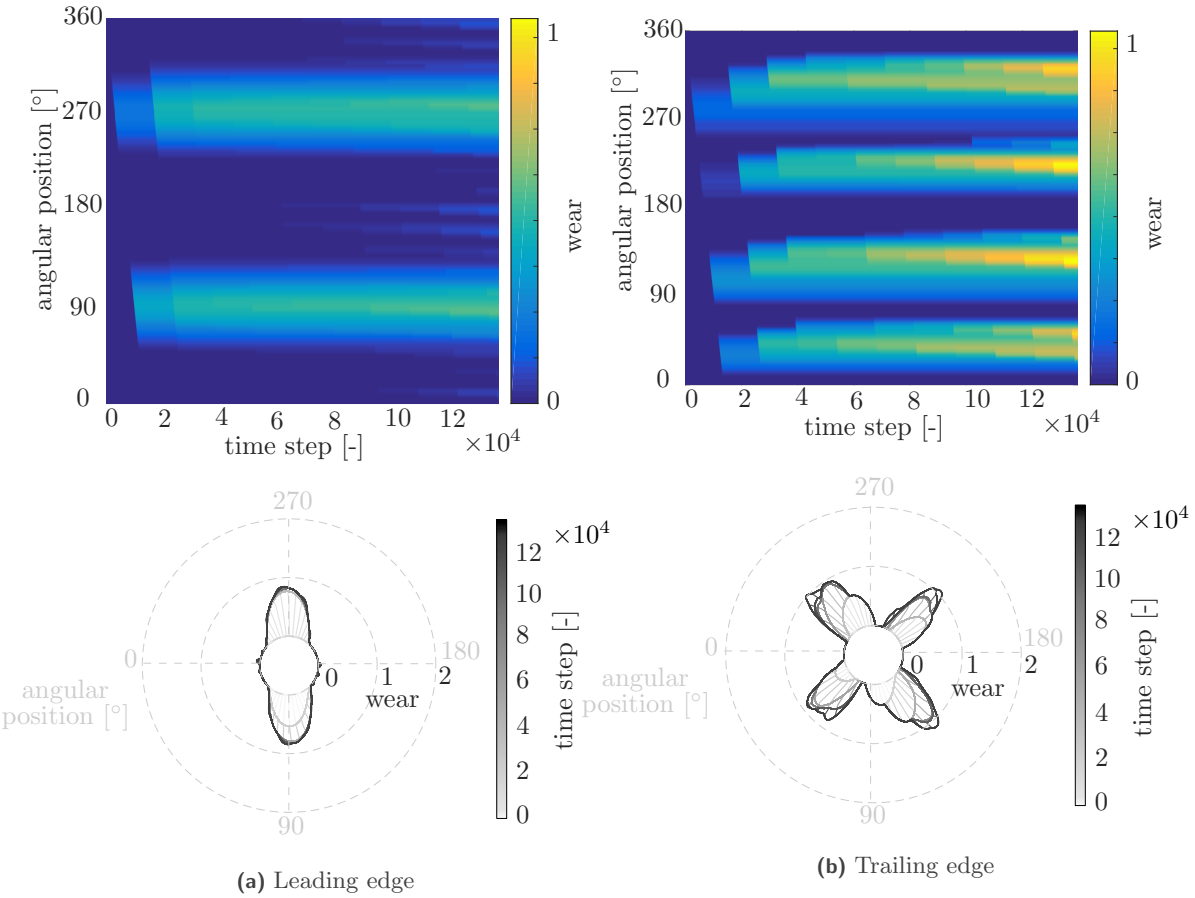

(a) Leading edge

(b) Trailing edge

Figure 12. Time evolution of the wear over the circumference of the abradable at the leading and trailing edges

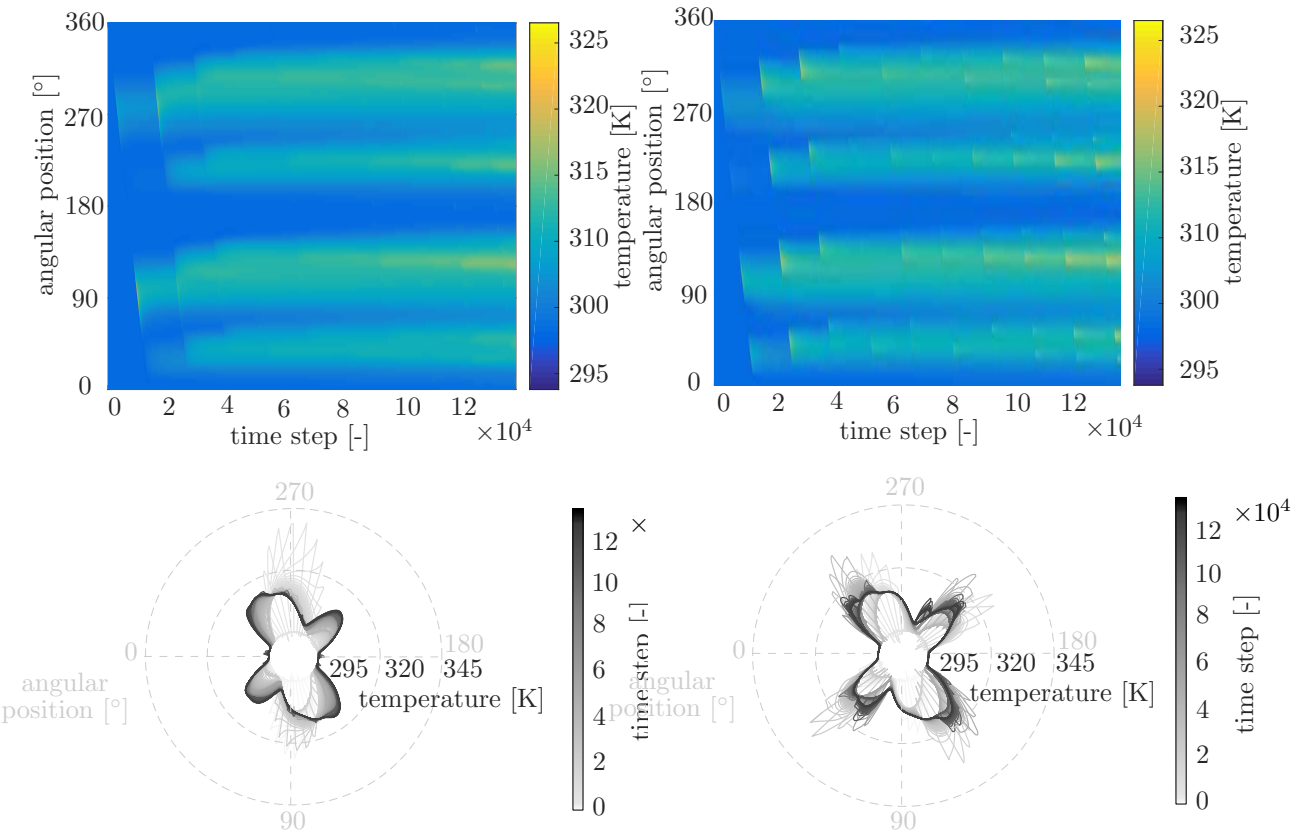

(a) Leading edge

(b) Trailing edge

Figure 13. Time evolution of the temperature over the circumference of the abradable at the leading and trailing edges

3 CONCLUSION

This paper investigates the numerical modeling of thermal effects in the abradable coating. A mechanical mesh consisting in independent two-node rod elements with elasto-plastic constitutive law is considered to compute the abradable wear. A thermal mesh of the abradable layer has been added to compute the evolution of the temperature in the abradable due to blade contacts. To reduce computation times of the temperature simulation, a different space and time discretization has been used. A convergence analysis has been performed which shows that the space discretization has low effect on the obtained results. The reduction of computation time can be done by considering a low number of abradable thermal elements. However, the time discretization has a larger effect due to conduction inside of the abradable.

In future works, the numerical model can be improved by considering temperature diffusion inside of the carter, providing carter dilatation. The two-dimensional model (tangential-axial) has to be extended to three dimensions (tangential-axial-radial). The thermal flux of the blade should also be calibrated using experiments to obtain a representative evolution of temperatures during rotor/stator interactions in real operating conditions. Moreover, a more accurate prediction of the blade heat flux could be to compute it as proportional to the friction between the blade and the abradable. Finally, a dependence of the mechanical property of the abradable coating with temperature should be included.

Acknowledgments

This research was supported by the Natural Sciences and Engineering Research Council of Canada (NSERC). The authors are also grateful to the industrial partner for supporting this project, Safran Aircraft Engines.

References

[1] Williams, R. J., 2011. "Simulation of blade casing interaction phenomena in gas turbines resulting from heavy tip rubs using an implicit time marching method". In Proceedings of the ASME Turbo Expo 2011 conference, GT2011-45495. doi: 10.1115/GT2011-45495 - oai: hal-01555287.

[2] Muszynska, A., Bently, D., Franklin, W., Hayashida, R., Kingsley, L., and Curry, A., 1989. Influence of rubbing on rotor dynamics - part 1. Tech. Rep. NAS8-36179, NASA. oai: 19890016092.

[3] Borel, M., Nicoll, A., Schlapfer, H., and Schmid, R., 1989. "The wear mechanisms occurring in abradable seals of gas turbines". *Surface & Coatings Technology,* **39**, pp. 117–126. doi: 10.1016/0257-8972(89)90046-7 - oai: hal-00627526.

[4] Mandard, R., Witz, J.-F., Boidin, X., Fabis, J., Desplanques, Y., and Meriaux, J., 2015. "Interacting force estimation during blade/seal rubs". *Tribology International,* **82**, pp. 504–513. doi: 10.1016/j.triboint.2014.01.026 - oai: hal-01093168.

[5] Legrand, M., Batailly, A., and Pierre, C., 2011. "Numerical investigation of abradable coating removal through plastic constitutive law in aircraft engine". *Journal of Computational and Nonlinear Dynamics,* **7**, pp. 011010–1–11. doi: 10.1115/1.4004951 - oai: hal-00627526.

[6] Sinha, S., 2005. "Non-linear dynamic response of a rotating radial timoshenko beam with periodic pulse loading at the free end". *International Journal of Non-Linear Mechanics,* **40**, pp. 113–149. doi: 10.1016/j.ijnonlinmec.2004.05.019.

[7] Lesaffre, N., Sinou, J. J., and Thouverez, F., 2007. "Stability analysis of rotating beams rubbing on an elastic circular structure". *Journal of Sound and Vibration,* **299**(4–5), pp. 1005–1032. doi: 10.1016/j.jsv.2006.08.027 - oai: arXiv:0801.3775.

[8] Legrand, M., Pierre, C., Cartraud, P., and Lombard, J.-P., 2009. "Two-dimensional modeling of an aircraft engine structural bladed disk-casing modal interaction". *Journal of Sound and Vibration,* **319**(1-2), pp. 366–391. doi: 10.1016/j.jsv.2008.06.019 - oai: hal-00328186v2.

[9] Salles, L., Blanc, L., Thouverez, F., and Gouskov, A., 2010. "Dynamic analysis of fretting wear in friction contact interfaces". *International Journal of Solids and Structures,* **48**(10), pp. 1513–1524. doi: 10.1016/j.ijsolstr.2011.01.035.

[10] Baïz, S., 2011. "Etude expérimentale du contact aube/abradable : contribution à la caractérisation mécanique des matériaux abradables et de leur interaction dynamique sur banc rotatif avec une aube". PhD thesis, Ecole Centrale de Lille. oai: tel-00605091.

[11] Millecamps, A., Brunel, J., Dufrénoy, P., Garcin, F., and Nucci, M., 2009. "Influence of thermal effects during blade-casing contact experiments". In Proceedings of the ASME 2009 IDETC & CIE conference, ASME. doi: 10.1115/DETC2009-86842 - oai: hal-01223060.

[12] Sternchüss, A., and Balmès, E., 2006. "On the reduction of quasi-cyclic disks with variable rotation speeds". *Proceedings of the International Conference on Advanced Acoustics and Vibration Engineering (ISMA)*, pp. 3925–3939. oai: hal-00266394.

[13] Kaptan, F., Panning-von Scheidt, L., and Wallaschek, J., 2015. "The vibrational behavior of coupled bladed disks with variable rotational speed". In Proceedings of the 86th Annual Meeting of the International Association of Applied Mathematics and Mechanics, pp. 255–256. doi: 10.1002/pamm.201510118.

[14] Laursen, T., 2002. *Computational contact and impact mechanics.* Springer.

[15] Wriggers, P., 2002. *Computational contact mechanics.* John Wiley & Sons.

[16] Adam, L., 2003. "Modélisation du comportement thermo-élasto-viscoplastique des métaux soumis à grandes déformations. application au formage superplastique.". Ph.D. thesis, Université de Liège, Liège, Belgium.

[17] Debard, Y., 2011. *Méthode des éléments finis : thermique*. Université du Mans.